Journal of Materials Chemistry A

Three-Dimensional Phase Evolution and Stress-Induced Non-Uniform Li Intercalation Behavior in Lithium Iron Phosphate

Journal:	*Journal of Materials Chemistry A*
Manuscript ID	TA-ART-10-2019-011697.R1
Article Type:	Paper
Date Submitted by the Author:	08-Dec-2019
Complete List of Authors:	Yang, Kaiqi; Rice University Tang, Ming; Rice University, Materials Science and NanoEngineering

Three-Dimensional Phase Evolution and Stress-Induced Non-Uniform Li Intercalation Behavior in Lithium Iron Phosphate

Kaiqi Yang[1] and Ming Tang[1, *]

1. Department of Materials Science & NanoEngineering, Rice University, Houston, TX 77005, USA.

[*] Corresponding author email: mingtang@rice.edu

Abstract

Lithium iron phosphate ($LiFePO_4$) olivine cathode displays rich phase transition behavior during charging/discharging. Despite extensive study, the evolution of the $LiFePO_4/FePO_4$ two-phase coexistence structure and the underlying mechanism is still a point of debate due to the intricate and often disparate phase morphologies observed. Here we apply phase-field simulation to provide detailed insights on the three-dimensional phase evolution process in $LiFePO_4$ upon delithiation under large driving force. Simulation reveals that the coherency stress arising from the $LiFePO_4/FePO_4$ lattice mismatch destabilizes the initially flat delithiation front and induces filamentary growth of $FePO_4$ phase along [010], which has excellent agreement with a recent operando X-ray imaging study [Ohmer et al. Nature Communications **6**, 6045 (2015)]. The combined simulation and experimental results provide the first illustration of the phenomenon of stress-induced instability of lithium (de)intercalation front in battery electrode compounds. We show that this phenomenon is facilitated by the surface mode of coherent spinodal decomposition in $LiFePO_4$ and influenced by the anisotropies of misfit strain, elasticity and lithium diffusion. It is detrimental to battery performance and life by causing stress concentration and reducing the lithium (de)intercalation kinetics and thus should be mitigated.

Introduction

Since its introduction by Padhi et al.[1] in 1997, $LiFePO_4$ has become a mainstream cathode material for Li-ion batteries due to its inherent safety, exceptional rate capability and low cost. Besides its commercial success, $LiFePO_4$ was also extensively studied for its rich and fascinating phase transition behavior, the fundamental understanding of which has broad implications for battery electrode materials that undergo electrochemically-driven phase transformations. Thermodynamically, $LiFePO_4$ undergoes a first-order phase transition between the Li-rich $Li_{1-x}FePO_4$ (LFP) and Li-poor Li_yFePO_4 (FP) phase upon Li (de)intercalation at room temperature, which are separated by a wide miscibility gap on the phase diagram[2,3]. However, phase evolution in $LiFePO_4$ from experimental observations upon cycling often deviates significantly from the equilibrium phase behavior, especially in nanosized particles and at high (dis)charging rates. Li solubility in LFP and FP phases is found to increase with decreasing particle size below 100 nm[4-7]. Recent in-operando X-ray-based measurements[8-12] confirm earlier predictions[13-15] that the equilibrium FP↔LFP transition could be bypassed by the formation of a metastable solid solution under high-rate charge/discharge. Such non-equilibrium phase behavior is closely related to the low energy barrier between LFP and FP[14,16], which can be relatively easily overcome by elastic energy[4,15] and surface reaction kinetics[13,17].

While the formation of metastable solid solution is believed to contribute to the remarkable rate performance of nanoscale $LiFePO_4$[18,19], conventional two-phase coexistence is still highly relevant in larger particles or nano-particles after rest[20] and has important implications for the material properties as it can result in fracture[21] and limited Li intercalation kinetics[22]. However, our understanding of the phase transition process in $LiFePO_4$ is challenged by the observation of many different phase morphologies such as (001)-oriented stripes [21,23],

(010)[24], (101)[12,25,26], (210)[27] and other high-index-plane phase boundaries[28-30], and core-shell structure[31,32]. Despite efforts to attribute such variety of phase morphologies to the loss of interface coherency[33], size effects[34] and kinetic competition between surface reaction and bulk diffusion[35], a unified picture remains to be developed. From the theoretical side, one aspect that receives much attention is how coherency stress arising from the lattice mismatch between FP and LFP influences phase evolution. A number of modeling studies attempt to elucidate the role of stress in experimental observed two-phase structure[15,33,34,36-39]. 3D phase-field simulations by Tang et al. [36] suggest that the observed phase boundary orientations in between (100) and (010)[28] could result from the compromise between elastic energy, which favors (100), and diffusion kinetics, which favors (010). Cogswell and Bazant[34] used a depth-average model to show that coherency stress could contribute to the formation of the stripe domain morphology seen in $LiFePO_4$ plates[21]. Theoretical study by Tang and Karma suggests that such periodic phase structure may result from a surface-mode coherent spinodal decomposition process induced by stress relaxation at free surface[40]. Abdellahi et al. show that the interplay between the anisotropies of interfacial energy and coherent strain in $LiFePO_4$ favors the (010) interface in equiaxed particles below 40 nm[37]. In a more recent work[15], 2D phase-field simulation that considers coherency stress produces a two-phase structure in $LiFePO_4$ plate-like particles that match the experiment well[12]. However, one complicating issue is that the experiments compared against the above mentioned modeling works were all performed ex-situ, which potentially allows the two-phase structure in $LiFePO_4$ particles to relax and equilibrate. It is not clear to what degree these observations reflect the dynamic phase evolution during charge/discharge. To this end, in-situ and in operando experiments are especially useful to resolve this concern.

Thanks to rapid advancement in characterization instruments and techniques, there are an

increasing number of in operando studies based on TEM[24,41], X-ray diffraction[9-11] and spectroscopic imaging[12,30,31,35,42] carried out in recent years to probe the phase behavior of $LiFePO_4$. They played a critical role in confirming the existence of metastable solid solution in nanosized $LiFePO_4$, and also provide valuable insights on the phase evolution kinetics in microsized particles. Among them, one notable experiment by Ohmer et al. is particularly revealing of the possible involvement of stress in phase evolution[30]. By applying scanning transmission x-ray microscopy (STXM) to track the spatiotemporal distribution of Fe oxidation state in a $LiFePO_4$ single crystal during delithiation, they observed that the growth of FP phase into the electrode is strongly non-uniform. After nucleating at electrode surface, FP domains grow much along [010] than the [100] direction, leading to filamentary domain morphology in the (001) cross section. The delithiation depth also exhibits significant variation along [001], and a wavy delithiation front with a periodicity of ~200nm is visible in the (100)-oriented 2D phase map obtained from STXM. The presence of non-flat (de)lithiation front in $LiFePO_4$ is not unique to this study and also seen in other in operando TXM experiments[31,35] though less pronounced. Ohmer et al. postulate that elastic effects are responsible for the non-uniform FP growth and Li intercalation behavior. However, no existing simulation has provided unequivocal support to this hypothesis to confirm the role of stress. A close examination of the complex phase morphology obtained from this STXM experiment necessitates 3D simulations, which are still few for $LiFePO_4$. Existing 3D simulations assume low overpotentials[36], open circuit condition[43], and/or small particle size[38,44], which do not match the experimental condition in Ref. [30] that involves high overpotential and large particle size.

In this work, we employ 3D phase-field simulation to study phase evolution in single crystalline $LiFePO_4$ upon delithiation under high overpotentials where the nucleation energy

barrier of FP phase is overcome by the large overpotentials and nucleation becomes spontaneous. Dynamic phase morphology from the simulation exhibits excellent agreement with the STXM experiment by Ohmer et al. [30]. Together, the experiment and simulation unambiguously elucidate the phenomenon of stress-induced destabilization of (de)lithiation front in battery electrodes. By providing a detailed look into the phase transition process in 3D, the simulation offers several significant insights beyond those available from the experiment. It shows that the initially uniform delithiation front is destabilized by a surface mode of coherent spinodal decomposition, and the misfit strain anisotropy controls the subsequent FP growth morphology. Furthermore, we discover that the phase morphology observed in Ref. [30] is only possible with the presence of antisite defects, which enhances Li transport along [100]/[001] and accelerates the relaxation of phase boundary morphology. The finding suggests that modifying Li diffusion anisotropy in $LiFePO_4$ with defect inclusion has considerable impact on the phase evolution pathway. The stress-induced non-uniform Li intercalation phenomenon has significant implications for the performance and degradation of battery electrodes that undergo phase separation upon charging/discharging. We show that it could lead to slow-down of the intercalation process and enhance stress concentration to promote fracture as observed in experiment. Further research on its mitigation is thus required.

Methodology

We employ the phase-field model developed for $LiFePO_4$ in Ref. [36] to carry out the simulations. In the model, the Li site occupancy fraction field c ($0<c<1$) is used to both describe the Li concentration distribution and distinguish between LFP and FP phases. The free energy of an $LiFePO_4$ particle is given by

$$F = \int_V \left[f_{chem}(c) + f_{el}(\epsilon_{ij}) + \frac{\kappa}{2}(\nabla c)^2 \right] dV \quad (1)$$

here f_{chem} represents the free energy density of Li_cFePO_4 with a uniform composition c and is described by a regular solution model

$$f_{chem} = \{RT[c\ln c + (1-c)\ln(1-c)] + \Omega c(1-c)]\}/V_m \quad (2)$$

where Ω = 12 kJ/mol is the regular solution coefficient that characterizes the phase separation behavior of $LiFePO_4$, V_m = 43.8 cm^3/mol is the molar volume of $LiFePO_4$, R is the gas constant and T = 298 K. According to Eq. 2 and as shown in Figure S1 in Supplementary Information (SI), there exists an energy barrier of 1303 J/mol between bulk LFP (c ≈ 1) and FP (c ≈ 0) phases at T = 298 K, which is close to the prediction of the first-principles calculations by Malik, Zhou and Ceder in Ref. 14. f_{el} is the elastic energy density given by linear elasticity:

$$f_{el} = \frac{1}{2} C_{ijkl}(\epsilon_{ij} - \epsilon^0_{ij}c)(\epsilon_{kl} - \epsilon^0_{kl}c) \quad (3)$$

where ϵ_{ij} = $(\partial u_j/\partial x_i + \partial u_i/\partial x_j)/2$ and u_i is the displacement vector. In Eq. 3, ϵ_{ij} is the total deformation tensor that characterizes the change of lattice constants of Li_cFePO_4 relative to the reference state ($FePO_4$). It contains two contributions, i.e. stress-induced elastic deformation and lattice expansion (or contraction) due to Li insertion (or extraction). The latter contribution is described by the transformation strain tensor $\epsilon^0_{ij}c$, which assumes the Vegard's law, i.e. that the lattice constants vary linearly with the Li concentration c. Here ϵ^0_{ij} is the misfit strain between stoichiometric $LiFePO_4$ and $FePO_4$, which are ϵ^0_{11}= 5%, ϵ^0_{22}= 3.6%, ϵ^0_{33}= -1.9% and zero for other tensor elements[45]. The difference between ϵ_{ij} and $\epsilon^0_{ij}c$ gives the elastic strain tensor. Because FP phase is chosen as the reference state, it has zero transformation strain but will be

elastically strained during phase transformation. The stiffness tensor C_{ijkl} is taken from the average values of $LiFePO_4$ and $FePO_4$ from first-principles calculations reported in Ref. 46.

The gradient energy $\kappa(\nabla c)^2/2$ contributes to the LFP/FP phase boundary energy. We choose $\kappa = 1.68 \times 10^{-12}$ J cm^{-1}, which produces an interface energy of 0.072 J m^{-2} that is the average of the (100), (010) and (001) phase boundary energies predicted by DFT calculations[37]. Given the free energy expression in Eq. 1, Li chemical potential in Li_cFePO_4 (per unit volume) is given by

$$\mu_{Li} = \frac{\delta F}{\delta c} = \frac{\partial f_{chem}}{\partial c} - C_{ijkl}\epsilon_{ij}^0(\epsilon_{kl} - \epsilon_{kl}^0 c) - \kappa\nabla^2 c \qquad 4)$$

The time evolution of the Li concentration field c is governed by the Cahn-Hilliard equation[47,48]

$$\frac{\partial c}{\partial t} = \nabla \cdot [\mathbf{M}c(1-c)\mu_{Li}] \qquad 5)$$

where **M** is the Li mobility tensor and related to the Li diffusivity through the Einstein relation, $M_{ij} = D_{ij}V_m/RT$. It is expressed in tensor form because Li exhibits anisotropic transport properties in $LiFePO_4$. Defect-free $LiFePO_4$ is predicted to be a one-dimensional Li diffuser[49], in which Li moves rapidly along [010] migration channels but has negligible diffusivity in other directions. However, both experiment[35,50] and modeling[51] show that antisite defects, which are common in battery compounds, increase the isotropy of Li diffusion in $LiFePO_4$ by impeding [010] transport but reducing the Li migration barriers along [100] and [001]. The $LiFePO_4$ single crystal studied by Ohmer et al. contains ~3% Fe_{Li} antisites and was observed to have two-dimensional Li diffusivity within the *bc* plane at an elevated temperature T = 440 K[50]. Recently, Hong et al. found that ~3% antisite defects is sufficient to produce comparable room-temperature Li diffusion coefficients of ~10^{-11} cm^2/s along [010] and [100]/[001] in microsized LFP particles [35]. For this reason, isotropic Li diffusivity D_{Li} = 10^{-11} cm^2/s is used in most simulations to be

consistent with the $LiFePO_4$ sample studied in Ref. [30]. This choice turns out to be a key factor in reproducing the experimental observation, which will be discussed below. 1D Li diffusivity is assumed in additional simulations to examine the effect of Li diffusion anisotropy on phase evolution.

The boundary conditions of Eq. 5 are given as follows. In simulations, the computational domain along [100] and [001] axes is assumed to be part of a larger electrode and periodic boundary conditions are applied for c and μ_{Li} on (100) and (001) domain surfaces. Similar to the electrode configuration in ref. [30], one (010) facet of the domain is assumed to be in contact with electrolyte with the Li flux given by the symmetric Butler-Volmer equation

$$j_{\mathrm{Li}} = \frac{V_{\mathrm{m}}}{F} j_0 \left[\exp\left(\frac{\left(\mu_{\mathrm{Li}}^{\mathrm{electrolyte}} - \mu_{\mathrm{Li}}^{\mathrm{surf}}\right)}{2RT/V_{\mathrm{m}}} \right) - \exp\left(- \frac{\left(\mu_{\mathrm{Li}}^{\mathrm{electrolyte}} - \mu_{\mathrm{Li}}^{\mathrm{surf}}\right)}{2RT/V_{\mathrm{m}}} \right) \right] \qquad 6)$$

While zero flux is imposed on the other (010) surface. $\mu_{\mathrm{Li}}^{\mathrm{electrolyte}}$ and $\mu_{\mathrm{Li}}^{\mathrm{surf}}$ are the chemical potentials of lithium in electrolyte and on electrode surface, respectively. $\mu_{\mathrm{Li}}^{\mathrm{electrolyte}}$ is controlled by the applied overpotential $\Delta\phi$ through the relation $\mu_{\mathrm{Li}}^{\mathrm{electrolyte}} = \mu_{\mathrm{Li}}^{\mathrm{eq}} - F\Delta\phi$, where F is the Faraday constant and $\mu_{\mathrm{Li}}^{\mathrm{eq}}$ is the Li chemical potential at LFP/FP two-phase equilibrium. The exchange current density j_0 is set to 1 A/m^2. In addition, natural boundary condition $\vec{n} \cdot \nabla c = 0$ is applied to both (010) surfaces.

In conjunction with Eqs. 4 and 5, we solve the stress equilibrium equation to determine the strain/stress distribution in the electrode:

$$\frac{\partial \sigma_{ij}}{\partial x_j} = \frac{\partial}{\partial x_j}\left[C_{ijkl}\left(\epsilon_{kl} - \epsilon_{kl}^0 c\right)\right] = 0 \qquad 7)$$

It can be seen that Eqs. 4, 5 and 7 couple the evolution of c and ϵ_{ij}. Eq. 7 is completed by traction-free boundary condition on (010) surfaces and zero displacement boundary condition on (100) and (001) surfaces.

In simulations, the governing equations are non-dimensionalized by length unit l_0 = 1 nm, energy unit $e_0 = 10^{-18}$ J and time unit $t_0 = l_0^5/M_{Li}e_0$. In the numerical implementation, Eq. 5 is solved by the finite-volume method and a semi-implicit real-space solver, and Eq. 7 is solved by a spectral iterative perturbation algorithm[52].

Results

We performed 3D phase-field simulation of the lithium deintercalation process in a single-crystalline $LiFePO_4$ electrode under a constant overpotential of 100 mV. The computational domain size is 256 × 128 × 256 nm along [100] (**a** axis), [010] (**b** axis) and [001] (**c** axis), respectively. Figure 1a shows a series of snapshots of phase evolution in the system during delithiation by visualizing only the FP phase ($c < 0.5$). Also see the animation of the simulation (Supplementary Movie 1) in SI. Figure 1b presents the (001) cross section of Li concentration distribution (shaded plane in Figure 1a). When delithiation starts, Li extraction from the electrode causes FP phase to first nucleate at the electrolyte-facing (010) surface. However, FP phase does not uniformly cover the electrode surface but forms many small individual surface islands, which latter coalesce into wedge-like domains. The FP wedges run in the <101> direction, which lies in the habit plane that has the minimum in-plane misfit strain between LFP and FP[15]. As delithiation proceeds, FP domains grow faster along [010] into the electrode than in the [100] direction, and the (010) electrode surface remains incompletely delithiated. The separate FP domains also coarsen during delithiation. As shown in Figure 1a and 1b, small FP

domains shrink and disappear while larger ones grow at their expense, resulting in a decrease in the number of individual FP domains with state of charge.

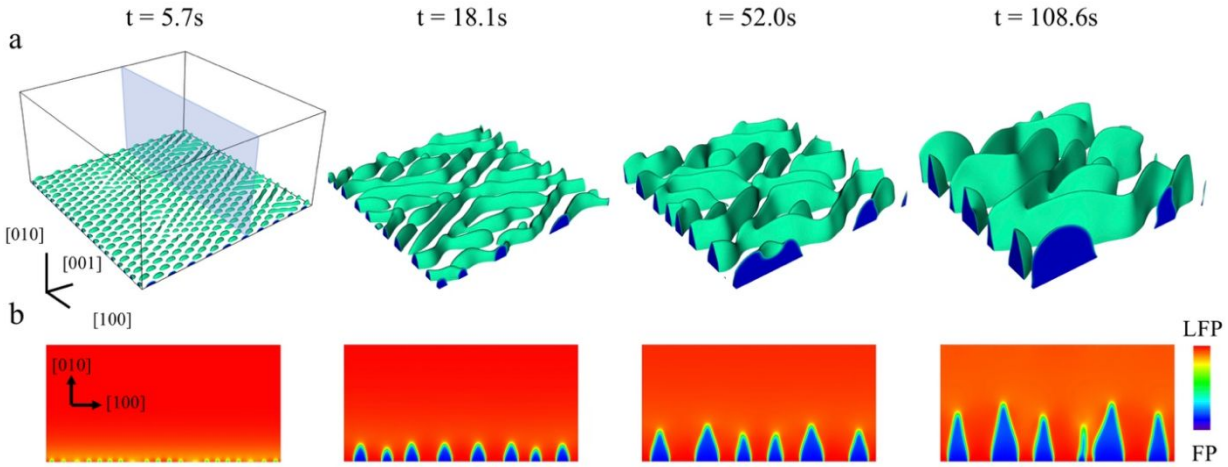

Figure 1. Phase evolution in a $LiFePO_4$ single crystal upon delithiation at a constant overpotential $\Delta\phi$ = 100 mV. a) FP phase morphology at different delithiation times. The region with $c > 0.5$ is made invisible in the snapshots. The box frame in the snapshot at t = 5.3 represents the computation domain ($L_{[100]} \times L_{[001]} \times L_{[010]}$ = 256 × 128 × 256 nm). b) Li concentration distribution on a (001) cross section indicated by the shaded plane shown in a).

When viewed from [001] direction, FP domains exhibit a spike morphology as shown in Figure 1b, which is remarkably similar to the observation of ref. [30]. In the STXM experiment by Ohmer et al., x-ray beam is parallel to the [100] axis of the $LiFePO_4$ single crystal. Because the obtained 2D spectroscopic images do not provide direct information on the phase distribution along [100], the [100] dimension of the FP phase is calculated from the spectroscopic data. The reconstructed (001) cross section of the FP domain thus represents the average of domain shapes along [100]. To facilitate comparison, we calculated the depth-averaged FP domain morphology from simulation results in a similar way. The domain is assumed to have a symmetric shape and its [100] dimension is calculated from the average Li concentration in the [100] direction. Figure

2 compares the simulated and experimental morphologies of the average FP domain in the (001) cross section as a function of state of charge (SOC), which are in very good agreement. Both simulation and experiment show that the FP phase maintains the filamentary morphology upon growth or shrinkage. The FP domain size in the simulation is about one tenth of that in the experiment due to computational constraint. However, the self-similar growth of the domain seen in simulation indicates that its morphology will persist to much larger domain sizes.

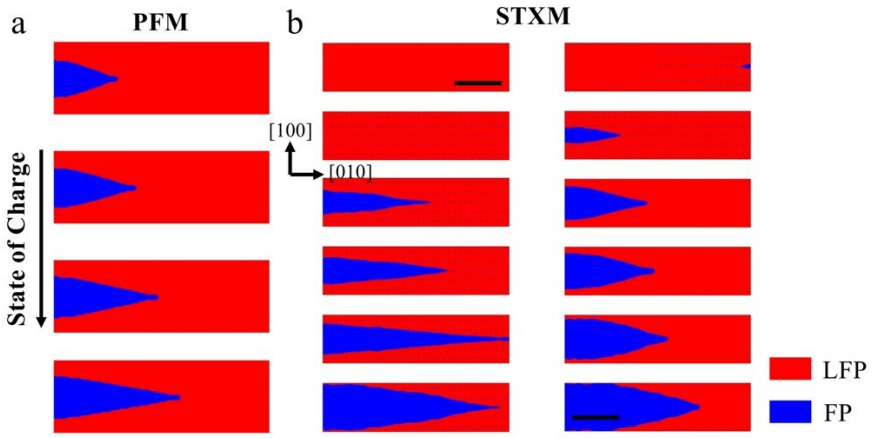

Figure 2. Comparison of the (001) cross sections of FP phase growth morphology from simulation and experiment. a) Simulated depth-averaged FP domain shape as a function of state of charge (SOC). b) SOC-dependent FP domain morphology from the operando STXM study. From ref. [30]. The left column is obtained from the delithiation process, and the right column is from the subsequent re-lithiation process.

When viewed from [100] direction, delithiation of the LFP electrode also shows strong inhomogeneity. Figure 3a visualizes the simulated 3D FP phase structure from this viewing angle. It shows that the wedge-like FP domains have wavy ridgelines with both “peaks” and “valleys”. Figure 3b presents a 2D phase map in the (100) plane constructed from the 3D simulation data. It represents the average FP phase fraction in the [100] direction and is analogous to the STXM image shown in Figure 3c. The simulated and experimental images again show close

resemblance. Like the experiment, the simulated 2D phase map also gives an impression of the existence of filament-like features in the delithiated region (highlighted by dotted lines). However, our 3D simulation provides additional insight on the nature of these filaments, which is not available from the depth-averaged STXM images. It shows that they are not really separate FP domains but rather represent regions with larger penetration depth of the FP phase that continuously extends in the [001] direction.

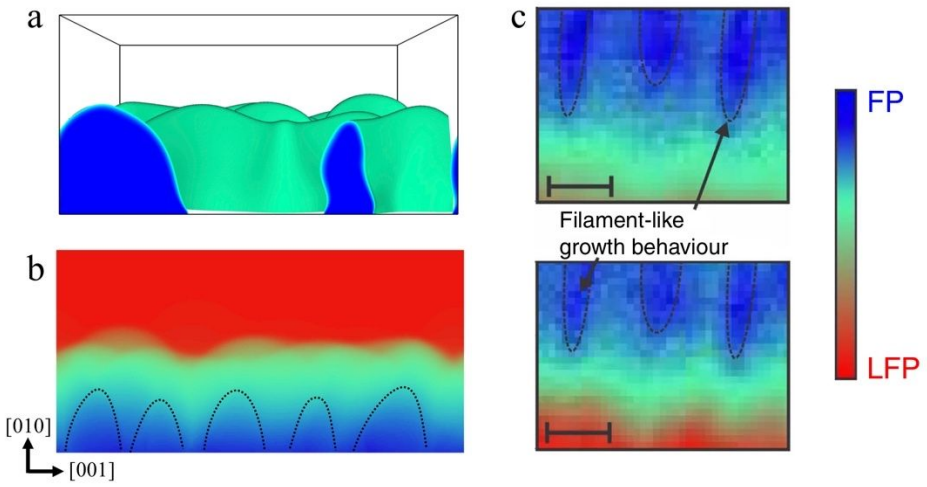

Figure 3. Comparison of the (100) cross sections of the FP phase growth morphology from simulation and experiment. a) 3D simulation at t = 128.4 s viewed from the [100] axis. b) 2D phase map calculated from the average FP phase fraction in the [100] direction. Filament-like features are outlined by dotted lines. c) Experimental STXM images also exhibit filament-like features within the FP-rich region. From ref. [30]. Note that FP phase grows from the bottom in the simulation and from the top in the experiment.

After establishing that our simulation faithfully reproduces the experimental results in ref. [30], we investigate whether coherency stress is responsible for the observed FP phase growth morphology. The delithiation process from both the experiment and simulation exhibits two prominent features, i.e. i) it proceeds into the LFP electrode in a strongly inhomogeneous way, which is exemplified by the non-uniform coverage of FP phase on the (010) surface, and ii) FP

domains maintains the filamentary morphology throughout delithiation. In simulation, these two features are absent when coherency stress is removed by assuming zero misfit strain between FP and LFP phases. As shown in Figure S2 in SI, FP phase would cover the entire (010) surface and grow uniformly into the electrode. The comparison confirms the enabling role of coherency stress in inducing the non-uniform delithiation and phase evolution behavior. We use simulation to further shed light on how stress and other relevant factors influence the phase evolution pathway. First, we examine in the details the early-stage destabilization of the delithiation front. Figure 4 shows the (001) cross section of the Li concentration field at the beginning of delithiation. It can be seen that Li extraction from the bottom (010) surface at first generates a uniform Li-poor surface layer. When LFP phase in the surface region reaches its metastability limit, a periodic composition modulation develops and amplifies on the (010) surface, which eventually causes the supersaturated Li_xFePO_4 solid solution to decompose into coexisting FP and LFP domains alternating along the surface. The flat delithiation front is destroyed by such lateral phase separation. However, phase separation does not occur inside the bulk of the electrode. This surface-localized phase separation behavior can be explained by a stress-related

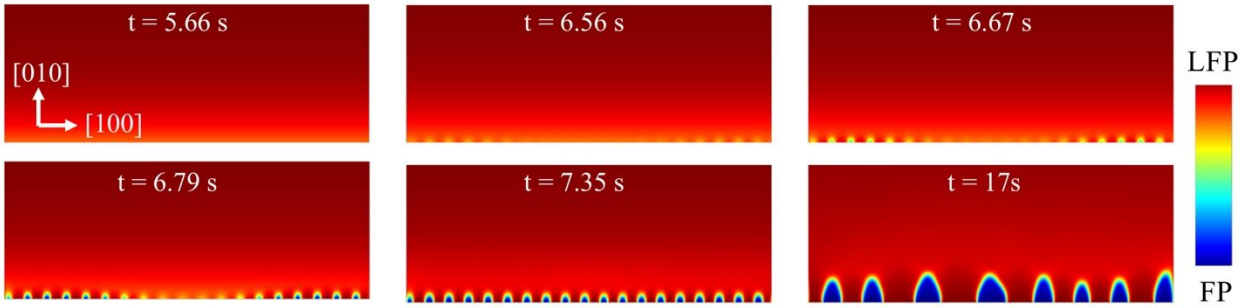

Figure 4. (001) cross section of the Li concentration field shows the initial formation of FP phase on (010) surface at the early stage of delithiation. Only the lower half of the computation domain is shown for clarity.

surface mode of coherent spinodal decomposition, which is revealed by our previous theoretical analysis[40]. For systems with composition-dependent lattice constants such as Li_xFePO_4, composition modulation incurs misfit strain energy, which suppresses or slows down phase separation. Because misfit stress can be effectively relaxed near free surface due to the traction-free boundary condition, phase separation will gain a larger driving force by preferentially developing parallel to the surface. This stress-induced phenomenon catalyzes the partial coverage of FP phase on the electrode surface and subsequent non-uniform growth. As a hallmark of the spinodal decomposition process[48], Figure 1a shows that the FP domains initially emerging on the surface exhibit an ordered spatial arrangement, which corresponds to the periodicity of the fastest-growing composition modulation wave of the surface-mode coherent spinodal. The periodic pattern is nonetheless lost at the later stage of phase evolution due to domain coalescence and coarsening. We note that the Li concentration gradient near surface created by Li extraction is not a necessary condition for the development of surface-localized phase separation. The surface-mode coherent spinodal decomposition still occurs when the system has a uniform composition[40].

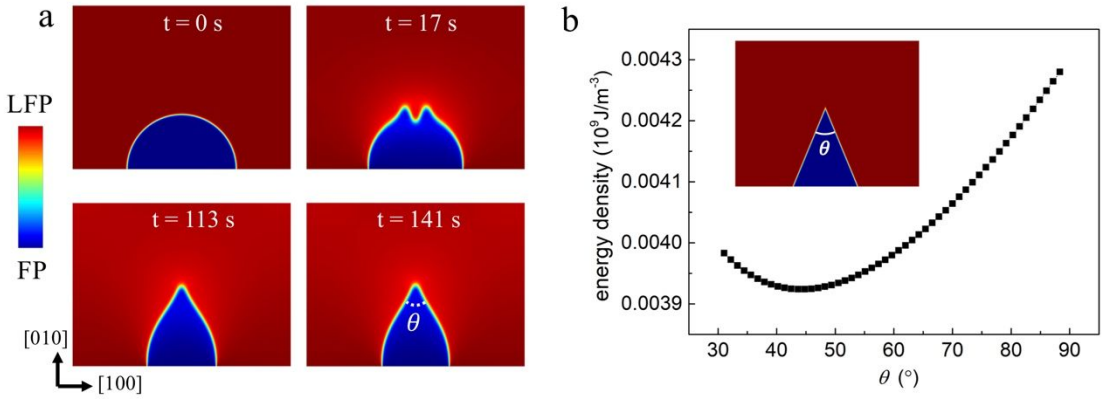

Figure 5 a) Morphological evolution of a FP phase domain under zero Li flux boundary condition. The domain initially has a semi-circular shape on the (001) plane. The domain shape stops evolving after t =

113 s, suggesting that the equilibrium morphology is reached. b) The average elastic energy density of the system as a function of θ of a triangular FP phase domain.

Next, we examine the growth process of FP domains that emerge from the initial phase separation stage. To shed light on the thermodynamic factors that contribute to the filamentary domain morphology of FP phase, we set up a 2D simulation in which a single FP domain is placed on the (010) surface of the LFP electrode and allowed to relax to its equilibrium morphology under zero flux boundary condition, i.e. no Li exchange between the system and electrolyte. As shown in Figure 5a, the initially semi-circular domain evolves to a stable filamentary shape similar to that from the delithiation simulation. This indicates that the FP domain morphology during delithiation is controlled by energetics. Compared to the elastic energy arising from the LFP/FP lattice mismatch, the LFP/FP interface energy accounts for a small fraction (23%) of the total energy of the equilibrated FP domain. Therefore, the domain morphology should be largely determined by the minimization of the elastic energy. To illustrate the relation between domain shape and misfit strain energy, we approximate the FP domain as a triangle with a variable angle θ embedded in the LFP phase (see Figure 5b inset) and calculate the elastic energy of the system assuming stoichiometry in both FP and LFP phases. Figure 5b shows the misfit strain energy as a function of θ. The elastic energy is minimized at $\theta = 44°$, which is close to the value (55°) obtained from the delithiation simulation.

Because isotropic misfit stress only results in isometric domain morphology, the filament-shaped FP domains directly reflects the anisotropy in the coherency stress field generated in $LiFePO_4$, which could be due to the anisotropic misfit strain and/or elastic moduli. The lattice mismatch between LFP and FP phases is strongly anisotropic, which is 5%, 3.6% and -2% along [100], [010] and [001] axes, respectively[45]. The elastic constants of LFP/FP also have

a moderate degree of anisotropy[46]. To examine the effect of misfit strain anisotropy, a series of simulations are performed, in which an FP surface domain evolves to its equilibrium morphology under different ratios of $\epsilon^0_{[100]}$ to $\epsilon^0_{[010]}$ while keeping $\epsilon^0_{[100]} + \epsilon^0_{[010]}$ constant. As shown in Figure 6a, the (001) cross section of the FP domain attains a semi-circular shape when $\epsilon^0_{[100]} = \epsilon^0_{[010]}$. It elongates along [010] when $\epsilon^0_{[100]}$ increases at the expense of $\epsilon^0_{[010]}$ (Figure 6b, c), and vice versa (Figure 6d, e). Clearly, the formation of [010]-aligned filamentary FP domains is due to the smaller misfit strain along [010], which encourages FP phase to grow in this direction to reduce the elastic strain energy that is analogous to the growth of plate-like or needle-like precipitates in some alloys[53]. We also examined the effect of the elastic anisotropy by comparing the FP phase morphology from simulations using the actual versus orientation-averaged elastic constants (Young's modulus E = 125.7 GPa, Poisson ratio ν = 0.252). The latter are taken from the Hill's empirical average of Li_xFePO_4's elastic moduli[54]. Comparison between Figure 6b and 6f shows that there is a relatively small difference in the domain shapes with and without the elastic anisotropy. On the other hand, the filamentary morphology cannot be reproduced in the absence of the anisotropy in lattice mismatch (Figure 6a). It can be concluded that the growth morphology of FP domains is controlled by the anisotropic misfit strain between FP and LFP, and to a lesser degree influenced by the anisotropy of the elastic moduli. It should be pointed out that the system does not need to have anisotropic misfit strain or elasticity to destabilize the uniform delithiation front through surface-mode coherent spinodal decomposition during the initial phase separation period. However, the LFP/FP misfit anisotropy further enhances the non-uniformity of the delithiation process by promoting the directional filamentary growth of FP phase.

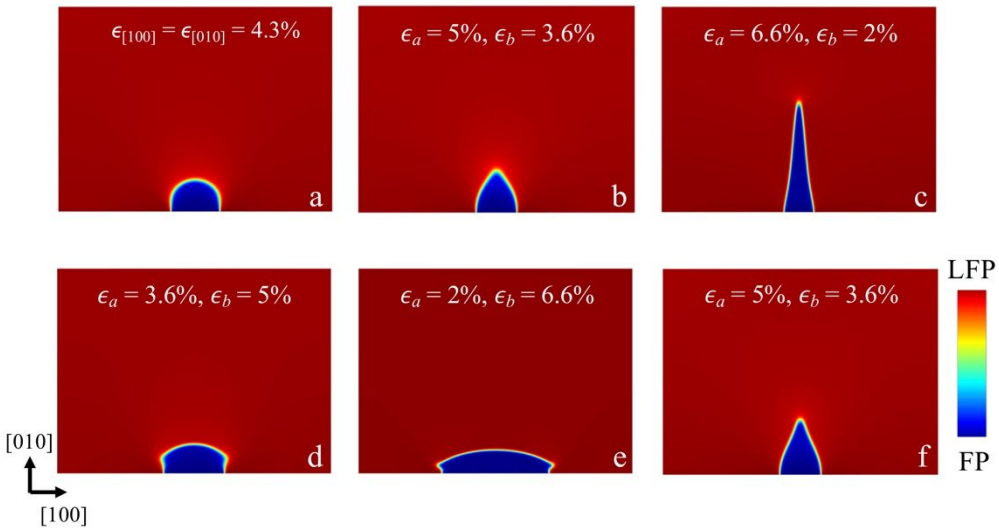

Figure 6. Effect of misfit strain and elastic anisotropy on the FP phase morphology. a-e) Equilibrium morphology of the FP domain assuming different values of $\epsilon_{[100]}$ and $\epsilon_{[010]}$ while $\epsilon_{[100]} + \epsilon_{[010]}$ is kept at constant. f) Equilibrium morphology of the FP domain assuming isotropic elastic constants E = 125.7 GPa and ν = 0.252.

In addition to the influence of coherency stress, we find that the Li diffusion anisotropy in Li_xFePO_4 also plays an important kinetic role in phase evolution. Specifically, we find that antisite-enhanced [100] Li diffusion[50,51,35] is essential to the formation of the experimentally observed FP filament morphology. DFT calculation by Morgan et al.[49] predicts that Li migration in Li_xFePO_4 is confined within one-dimensional channels along [010], a feature that has since been usually associated with this material. However, the filamentary FP domain morphology does not form when 1D Li diffusivity is assumed in simulation. As shown in Figure 7, a system with 1D Li diffusion undergoes a similar surface-localized phase separation as in the case of isotropic Li diffusivity. Here the composition modulation along [100] is achieved by Li movement within the [010] channels, which also induces phase separation along [010]. However, phase evolution at the later growth stage differs considerably between the two cases. With 1D Li diffusivity, FP domains obtain Y-shaped and hockey-stick-shaped shapes instead of filament

morphology. They result from incomplete coalescence of neighboring FP domains, and the irregular morphology persists as delithiation proceeds. The difference between the cases of 1D vs isotropic Li diffusivity is of kinetic origin. The evolution of FP domains towards their equilibrium morphology requires Li redistribution within and between FP domains aligned in the [100] direction, but the 1D Li transport in defect-lean $LiFePO_4$ places a stringent restriction on Li movement and thus impedes the phase evolution kinetics. Because antisite defects enhance the [100] Li diffusivity in $LiFePO_4$ [35,51], they help accelerate phase evolution towards the equilibrium two-phase morphology even though they reduce the Li diffusivity along the [010] fast migration direction at the same time. The observation of filamentary FP domains in the LFP single crystal in ref. [30] is consistent with its antisite content[50]. Similar defect level and reduced Li diffusion anisotropy have also been reported for $LiFePO_4$ particles prepared by the more common hydrothermal synthesis method[35]. Therefore, the phase evolution behavior revealed in ref. [30] and this work could have broad relevance.

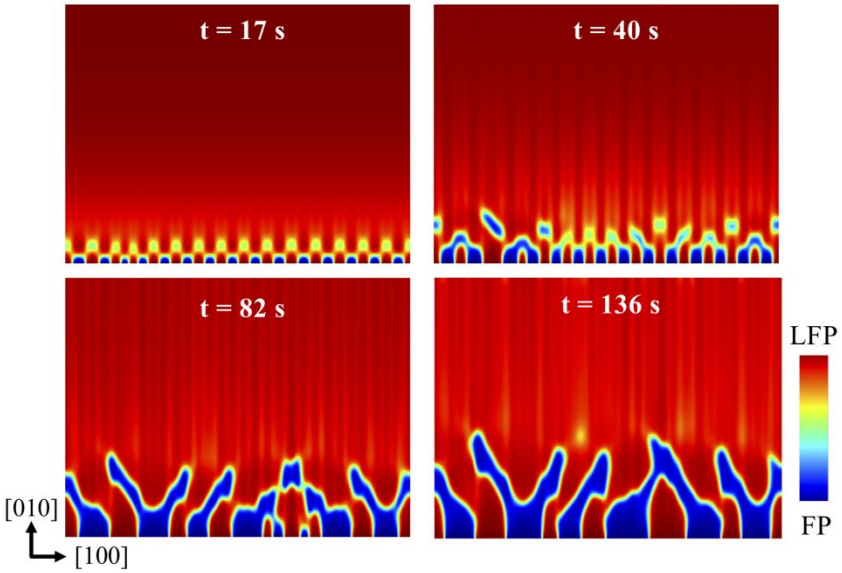

Figure 7. Phase evolution in $LiFePO_4$ with 1D Li diffusivity upon delithiation at a constant overpotential $\Delta\phi$ = 100 mV.

Discussion

Despite the very good agreement in the phase growth morphology, a notable difference exists between the experimental observation of Ohmer et al. [30] and our simulation: the FP domains are found to first form at the interface between current collector (CC) and LFP electrode in the experiment, but they nucleate at the electrode/electrolyte interface in the phase-field simulations. This difference results from the different electron conduction pathways in the experimental sample and assumed in the simulations. First-principles calculation predicts a strong binding energy between polaron and Li ion in $LiFePO_4$[55]. Li^+ and e^- thus tend to co-migrate as a neutral complex in $LiFePO_4$ [56]. Such behavior is expected in conventional porous electrodes. Because of the low intrinsic electronic conductivity of $LiFePO_4$, electrons will mainly migrate through conductive additives in the porous electrode and couple with Li ions at the $LiFePO_4$ particle surface before entering into the particles. In contrast, the electrode studied by Ohmer et al. has a very different configuration and is made of a monolithic LFP single crystal sandwiched between CC and solid electrolyte. As such, e^- and Li^+ are forced to enter/leave the electrode on the opposite sides of the LFP single crystal, i.e. at the CC/electrode and electrolyte/electrode interfaces, respectively, and cannot co-migrate within $LiFePO_4$. It is speculated in ref. [30] that Ga doping during the focused-ion-beam fabrication of the LFP electrode has the donor effect to increase the ionic and decrease the electronic conductivity in $LiFePO_4$, which causes the FP phase to first form on the CC side of the electrode. Since this is not an intrinsic property of $LiFePO_4$ and porous electrodes are most relevant for practical applications, the co-migration of Li^+ and e^- in $LiFePO_4$ is assumed in our simulation, and the diffusivity value used corresponds to that of the Li^+–e^- complex.

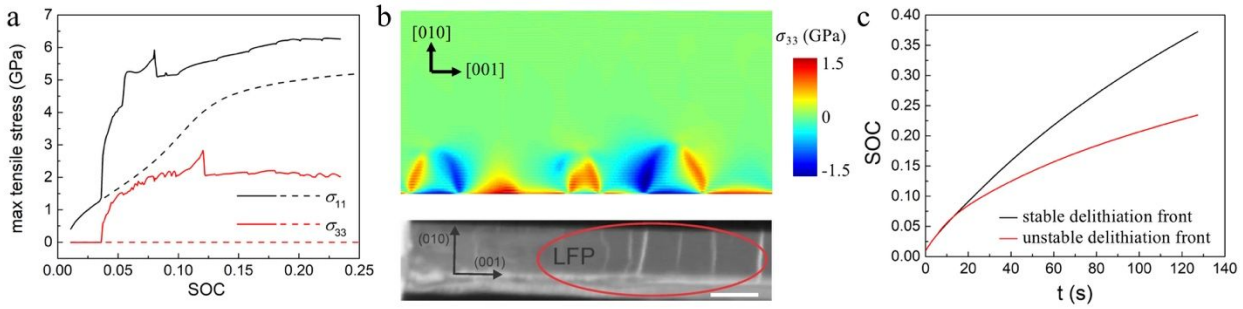

Figure 8. Effect of the destabilization of the delithiation front in $LiFePO_4$ on stress evolution and delithiation rate. a) Maximal tensile stress along [100] (σ_{11}) and [001] (σ_{33}) as a function of SOC in the original simulation (solid lines) and the controlled simulation (dashed lines) that maintains a uniform delithiation front. b) A (100) cross section of the σ_{33} field in the original simulation at t = 52 s (top) and the STXM image from ref. [30] showing the presence of cracks in $LiFePO_4$ (bottom). c) SOC vs time upon delithiation at a constant overpotential $\Delta\phi$ = 100 mV in the original (red) and controlled (black) simulations.

The development of non-uniform (de)lithiation front inside electrode particles is detrimental to battery life and performance by causing stress concentration and reducing the Li intercalation rate. To demonstrate this, we compare the internal stress and delithiation rate between the original simulation and a "controlled" simulation, in which a uniform delithiation front is maintained throughout the delithiation process by reducing the [100] and [001] dimensions of the computation domain to suppress composition modulation along these directions. Figure 8a shows that the maximum tensile stress along [100] and [001] (σ_{11} and σ_{33}, respectively) in the original simulation rises abruptly after the delithiation front is destabilized at SOC ≈ 0.04. Figure 8b shows that large tensile σ_{33} develops at the electrode surface, which is responsible for triggering extensive crack growth in the $LiFePO_4$ crystal as observed in the operando STXM experiment[30]. In contrast, σ_{33} is purely compressive in the electrode in the

control simulation, i.e. a uniform delithiation front will prevent crack formation in the (001) plane, and σ_{11} also remains at lower level than in the original simulation. A uniform Li intercalation front also facilitates faster delithiation. As shown in Figure 8c, while the delithiation rate is similar at first in the two simulations, Li extraction slows down significantly after composition non-uniformity develops in the original simulation. The SOC of the electrode in the controlled simulation is 59% higher than in the original simulation when the latter is terminated at t = 127 s. The development of non-uniform (de)lithiation front in electrode particles has been observed in other electrode materials[57,58] besides $LiFePO_4$ and is likely to be a common phenomenon during battery cycling. Its occurrence could be even more prominent in solid-state batteries, in which the increased stress level further exacerbates interface instability[59]. As our study shows here, this phenomenon is detrimental to battery life and performance and demands close attention in future research.

Conclusions

Phase evolution in $LiFePO_4$ during the delithiation process under a large overpotential is studied in 3D phase-field simulations in this work. The simulated growth morphology of FP phase exhibits very good agreement with a previous operando STXM experiment[30] and reveals a strongly non-uniform delithiation front characterized by the filamentary growth of FP phase and spatially modulated delithiation depth. Our simulations elucidate the mechanism underlying the observed non-uniform delithiation behavior in $LiFePO_4$ with the following conclusions being reached. First, the flat delithiation front is destabilized by a surface-localized phase separation process, which is induced by the coherency stress present in the electrode. Second, the experimentally observed filamentary FP domains result from the anisotropy in the misfit strain

between FP and LFP phases and to a lesser degree the elasticity anisotropy, which prefers the FP phase to grow in the [010] direction. Third, the Li diffusion anisotropy in $LiFePO_4$, which can be modified by antisite defects, has a large impact on the phase evolution morphology. The observed filamentary growth of FP phase is dependent on antisite-enhanced Li diffusion along [100] and will not appear in defect-free $LiFePO_4$. Last, the stress-induced non-uniform delithiation behavior in $LiFePO_4$ could adversely affect the electrode by increasing the internal stress and reducing the Li (de)intercalation rate.

Acknowledgments

KY and MT are supported by DOE under project number DE-SC0019111. Simulations were performed on supercomputers at the Texas Advanced Computing Center (TACC) at The University of Texas and the National Energy Research Scientific Computing Center, a DOE Office of Science User Facility supported by the Office of Science of the U.S. Department of Energy under Contract No. DE-AC02-05CH11231.

References

1 Padhi, A. K., Nanjundaswamy, K. S. & Goodenough, J. B. Phospho-olivines as positive-electrode materials for rechargeable lithium batteries. *J. Electrochem. Soc.* **144**, 1188 (1997).

2 Dodd, J. L., Yazami, R. & Fultz, B. Phase diagram of Li_xFePO_4. *Electrochem. Solid-State Lett.* **9**, A151 (2006).

3 Zhou, F., Maxisch, T. & Ceder, G. Configurational electronic entropy and the phase diagram of mixed-valence oxides: the case of Li_xFePO_4. *Phys. Rev. Lett.* **97** (2006).

4 Meethong, N., Huang, H.-Y. S., Carter, W. C. & Chiang, Y.-M. Size-dependent lithium miscibility gap in nanoscale $Li_{1-x}FePO_4$. *Electrochem. Solid-State Lett.* **10**, A134 (2007).

5 Yamada, A., Koizumi, H., Nishimura, S., Sonoyama, N., Kanno, R., Yonemura, M., Nakamura, T. & Kobayashi, Y. Room-temperature miscibility gap in Li_xFePO_4. *Nat. Mater.* **5**, 357 (2006).

6 Gibot, P., Casas-Cabanas, M., Laffont, L., Levasseur, S., Carlach, P., Hamelet, S., Tarascon, J. M. & Masquelier, C. Room-temperature single-phase Li insertion/extraction in nanoscale Li_xFePO_4. *Nat. Mater.* **7**, 741 (2008).

7 Ichitsubo, T., Doi, T., Tokuda, K., Matsubara, E., Kida, T., Kawaguchi, T., Yagi, S., Okada, S. & Yamaki, J. What determines the critical size for phase separation in $LiFePO_4$ in lithium ion batteries? *J. Mater. Chem. A* **1**, 14532 (2013).

8 Sharma, N., Guo, X., Du, G., Guo, Z., Wang, J., Wang, Z. & Peterson, V. K. Direct evidence of concurrent solid-solution and two-phase reactions and the nonequilibrium structural evolution of $LiFePO_4$. *J. Am. Chem. Soc.* **134**, 7867 (2012).

9 Liu, H., Strobridge, F. C., Borkiewicz, O. J., Wiaderek, K. M., Chapman, K. W., Chupas, P. J. & Grey, C. P. Capturing metastable structures during high-rate cycling of $LiFePO_4$ nanoparticle electrodes. *Science* **344**, 1252817 (2014).

10 Zhang, X., van Hulzen, M., Singh, D. P., Brownrigg, A., Wright, J. P., van Dijk, N. H. & Wagemaker, M. Rate-induced solubility and suppression of the first-order phase transition in olivine $LiFePO_4$. *Nano Lett.* **14**, 2279 (2014).

11 Hess, M., Sasaki, T., Villevieille, C. & Novak, P. Combined operando X-ray diffraction-electrochemical impedance spectroscopy detecting solid solution reactions of $LiFePO_4$ in batteries. *Nat. Commun.* **6**, 8169 (2015).

12 Lim, J., Li, Y. Y., Alsem, D. H., So, H., Lee, S. C., Bai, P., Cogswell, D. A., Liu, X. Z., Jin, N., Yu, Y. S., Salmon, N. J., Shapiro, D. A., Bazant, M. Z., Tyliszczak, T. & Chueh, W. C. Origin and hysteresis of lithium compositional spatiodynamics within battery primary particles. *Science* **353**, 566 (2016).

13 Bai, P., Cogswell, D. A. & Bazant, M. Z. Suppression of phase separation in $LiFePO_4$ nanoparticles during battery discharge. *Nano Lett.* **11**, 4890 (2011).

14 Malik, R., Zhou, F. & Ceder, G. Kinetics of non-equilibrium lithium incorporation in $LiFePO_4$. *Nat. Mater.* **10**, 587 (2011).

15 Cogswell, D. A. & Bazant, M. Z. Coherency strain and the kinetics of phase separation in $LiFePO_4$ nanoparticles. *ACS Nano* **6**, 2215 (2012).

16 Abdellahi, A., Akyildiz, O., Malik, R., Thornton, K. & Ceder, G. The thermodynamic stability of intermediate solid solutions in $LiFePO_4$ nanoparticles. *J. Mater. Chem. A* **4**, 5436 (2016).

17 Bazant, M. Z. Thermodynamic stability of driven open systems and control of phase separation by electro-autocatalysis. *Faraday Discuss.* **199**, 423 (2017).
18 Chung, S. Y., Bloking, J. T. & Chiang, Y. M. Electronically conductive phospho-olivines as lithium storage electrodes. *Nat. Mater.* **1**, 123 (2002).
19 Kang, B. & Ceder, G. Battery materials for ultrafast charging and discharging. *Nature* **458**, 190 (2009).
20 Li, Y. Y., Chen, H. R., Lim, K., Deng, H. D., Lim, J., Fraggedakis, D., Attia, P. M., Lee, S. C., Jin, N., Moskon, J., Guan, Z. X., Gent, W. E., Hong, J., Yu, Y. S., Gaberscek, M., Islam, M. S., Bazant, M. Z. & Chueh, W. C. Fluid-enhanced surface diffusion controls intraparticle phase transformations. *Nat. Mater.* **17**, 915 (2018).
21 Chen, G., Song, X. & Richardson, T. J. Electron microscopy study of the $LiFePO_4$ to $FePO_4$ phase transition. *Electrochem. Solid-State Lett.* **9**, A295 (2006).
22 Weichert, K., Sigle, W., van Aken, P. A., Jamnik, J., Zhu, C., Amin, R., Acarturk, T., Starke, U. & Maier, J. Phase boundary propagation in large $LiFePO_4$ single crystals on delithiation. *J. Am. Chem. Soc.* **134**, 2988 (2012).
23 Zhang, X., van Hulzen, M., Singh, D. P., Brownrigg, A., Wright, J. P., van Dijk, N. H. & Wagemaker, M. Direct view on the phase evolution in individual $LiFePO_4$ nanoparticles during Li-ion battery cycling. *Nat. Commun.* **6**, 8333 (2015).
24 Zhu, Y., Wang, J. W., Liu, Y., Liu, X., Kushima, A., Liu, Y., Xu, Y., Mao, S. X., Li, J., Wang, C. & Huang, J. Y. In situ atomic-scale imaging of phase boundary migration in $FePO_4$ microparticles during electrochemical lithiation. *Adv. Mater.* **25**, 5461 (2013).
25 Ramana, C. V., Mauger, A., Gendron, F., Julien, C. M. & Zaghib, K. Study of the Li-insertion/extraction process in $LiFePO_4/FePO_4$. *J. Power Sources* **187**, 555 (2009).
26 Boesenberg, U., Meirer, F., Liu, Y., Shukla, A. K., Dell'anna, R., Tyliszczak, T., Chen, G., Andrews, J. C., Richardson, T. J., Kostecki, R. & Cabana, J. Mesoscale phase distribution in single particles of $LiFePO_4$ following lithium deintercalation. *Chem. Mater.* **25**, 1664 (2013).
27 Kobayashi, S., Kuwabara, A., Fisher, C. A. J., Ukyo, Y. & Ikuhara, Y. Microscopic mechanism of biphasic interface relaxation in lithium iron phosphate after delithiation. *Nat. Commun.* **9** (2018).
28 Laffont, L., Delacourt, C., Gibot, P., Wu, M. Y., Kooyman, P., Masquelier, C. & Tarascon, J. M. Study of the $LiFePO_4/FePO_4$ two-phase system by high-resolution electron energy loss spectroscopy. *Chem. Mater.* **18**, 5520 (2006).
29 Yu, Y. S., Kim, C., Shapiro, D. A., Farmand, M., Qian, D., Tyliszczak, T., Kilcoyne, A. L., Celestre, R., Marchesini, S., Joseph, J., Denes, P., Warwick, T., Strobridge, F. C., Grey, C. P., Padmore, H., Meng, Y. S., Kostecki, R. & Cabana, J. Dependence on crystal size of the nanoscale chemical phase distribution and fracture in Li_xFePO_4. *Nano Lett.* **15**, 4282 (2015).
30 Ohmer, N., Fenk, B., Samuelis, D., Chen, C. C., Maier, J., Weigand, M., Goering, E. & Schutz, G. Phase evolution in single-crystalline $LiFePO_4$ followed by in situ scanning X-ray microscopy of a micrometre-sized battery. *Nat. Commun.* **6**, 6045 (2015).
31 Wang, J., Karen Chen-Wiegart, Y. C., Eng, C., Shen, Q. & Wang, J. Visualization of anisotropic-isotropic phase transformation dynamics in battery electrode particles. *Nat. Commun.* **7**, 12372 (2016).
32 Nakamura, A., Furutsuki, S., Nishimura, S., Tohei, T., Sato, Y., Shibata, N., Yamada, A. & Ikuhara, Y. Phase boundary structure of Li_xFePO_4 cathode material revealed by

atomic-resolution scanning transmission electron microscopy. *Chem. Mater.* **26**, 6178 (2014).
33 Heo, T. W., Tang, M., Chen, L. Q. & Wood, B. C. Defects, entropy, and the stabilization of alternative phase boundary orientations in battery electrode particles. *Adv. Energy Mater.* **6** (2016).
34 Cogswell, D. A. & Bazant, M. Z. Size-dependent phase morphologies in $LiFePO_4$ battery particles. *Electrochem. Commun.* **95**, 33 (2018).
35 Hong, L., Li, L., Chen-Wiegart, Y. C., Wang, J., Xiang, K., Gan, L., Li, W., Meng, F., Wang, F., Wang, J., Chiang, Y.-M., Jin, S. & Tang, M. 2D Li diffusion behavior and probable hybrid phase transformation kinetics in olivine lithium iron phosphate. *Nat. Commun.* **8**, 1194 (2017).
36 Tang, M., Belak, J. F. & Dorr, M. R. Anisotropic phase boundary morphology in nanoscale olivine electrode particles. *J. Phys. Chem. C* **115**, 4922 (2011).
37 Abdellahi, A., Akyildiz, O., Malik, R., Thornton, K. & Ceder, G. Particle-size and morphology dependence of the preferred interface orientation in $LiFePO_4$ nano-particles. *J. Mater. Chem. A* **2**, 15437 (2014).
38 Nadkarni, N., Rejovitsky, E., Fraggedakis, D., Di Leo, C. V., Smith, R. B., Bai, P. & Bazant, M. Z. Interplay of phase boundary anisotropy and electro-auto-catalytic surface reactions on the lithium intercalation dynamics in Li_xFePO_4 plateletlike nanoparticles. *Phys. Rev. Mater.* **2** (2018).
39 Ichitsubo, T., Tokuda, K., Yagi, S., Kawamori, M., Kawaguchi, T., Doi, T., Oishi, M. & Matsubara, E. Elastically constrained phase-separation dynamics competing with the charge process in the $LiFePO_4/FePO_4$ system. *J. Mater. Chem. A* **1**, 2567 (2013).
40 Tang, M. & Karma, A. Surface modes of coherent spinodal decomposition. *Phys. Rev. Lett.* **108** (2012).
41 Niu, J., Kushima, A., Qian, X., Qi, L., Xiang, K., Chiang, Y. M. & Li, J. In situ observation of random solid solution zone in $LiFePO_4$ electrode. *Nano Lett.* **14**, 4005 (2014).
42 Wang, J., Chen-Wiegart, Y. C. & Wang, J. In operando tracking phase transformation evolution of lithium iron phosphate with hard X-ray microscopy. *Nat. Commun.* **5**, 4570 (2014).
43 Heo, T. W., Chen, L. Q. & Wood, B. C. Phase-field modeling of diffusional phase behaviors of solid surfaces: A case study of phase-separating Li_XFePO_4 electrode particles. *Comput.Mater. Sci.* **108**, 323 (2015).
44 Welland, M. J., Karpeyev, D., O'Connor, D. T. & Heinonen, O. Miscibility gap closure, interface morphology, and phase microstructure of 3D Li_xFePO_4 nanoparticles from surface wetting and coherency strain. *Acs Nano* **9**, 9757 (2015).
45 Meethong, N., Huang, H. Y. S., Speakman, S. A., Carter, W. C. & Chiang, Y. M. Strain accommodation during phase transformations in olivine-based cathodes as a materials selection criterion for high-power rechargeable batteries. *Adv. Funct. Mater.* **17**, 1115 (2007).
46 Maxisch, T. & Ceder, G. Elastic properties of olivine $Li_xFePO_4$from first principles. *Phys. Rev. B* **73** (2006).
47 Cahn, J. W. & Hilliard, J. E. Free energy of a nonuniform system .1. interfacial free energy. *J. Chem. Phys.* **28**, 258 (1958).
48 Cahn, J. W. On spinodal decomposition. *Acta Metall.* **9**, 795 (1961).

49 Morgan, D., Van der Ven, A. & Ceder, G. Li conductivity in Li_xMPO_4 (M = Mn, Fe, Co, Ni) olivine materials. *Electrochem. Solid-State Lett.* **7**, A30 (2004).

50 Amin, R., Balaya, P. & Maier, J. Anisotropy of electronic and ionic transport in $LiFePO_4$ single crystals. *Electrochem. Solid-State Lett.* **10** (2007).

51 Malik, R., Burch, D., Bazant, M. & Ceder, G. Particle size dependence of the ionic diffusivity. *Nano Lett.* **10**, 4123 (2010).

52 Wang, J. J., Bhattacharyya, S., Li, Q., Heo, T. W., Ma, X. Q. & Chen, L.-Q. Elastic solutions with arbitrary elastic inhomogeneity and anisotropy. *Philos. Mag. Lett.* 1 (2012).

53 Balluffi, R. W., Allen, S. M. & Carter, W. C. *Kinetics of Materials*. (John Wiley & Sons, 2005).

54 Hill, R. The elastic behaviour of a crystalline aggregate. *Proc. Phys. Soc. London, Sect. A* **65**, 349 (1952).

55 Maxisch, T., Zhou, F. & Ceder, G. *Ab initio* study of the migration of small polarons in olivine Li_xFePO_4 and their association with lithium ions and vacancies. *Phys. Rev. B* **73** (2006).

56 Malik, R., Abdellahi, A. & Ceder, G. A critical review of the Li insertion mechanisms in $LiFePO_4$ electrodes. *J. Electrochem. Soc.* **160**, A3179 (2013).

57 Ulvestad, A., Singer, A., Cho, H. M., Clark, J. N., Harder, R., Maser, J., Meng, Y. S. & Shpyrko, O. G. Single particle nanomechanics in operando batteries via lensless strain mapping. *Nano Lett.* **14**, 5123 (2014).

58 Gent, W. E., Li, Y., Ahn, S., Lim, J., Liu, Y., Wise, A. M., Gopal, C. B., Mueller, D. N., Davis, R., Weker, J. N., Park, J. H., Doo, S. K. & Chueh, W. C. Persistent state-of-charge heterogeneity in relaxed, partially charged $Li_{1-x}Ni_{1/3}Co_{1/3}Mn_{1/3}O_2$ secondary particles. *Adv. Mater.* **28**, 6631 (2016).

59 Bucci, G., Talamini, B., Balakrishna A. R., Chiang, Y.-M. & Carter, W. C. Mechanical instability of electrode-electrolyte interfaces in solid state batteries. *Phys. Rev. Mater.* **2**, 105407 (2018).

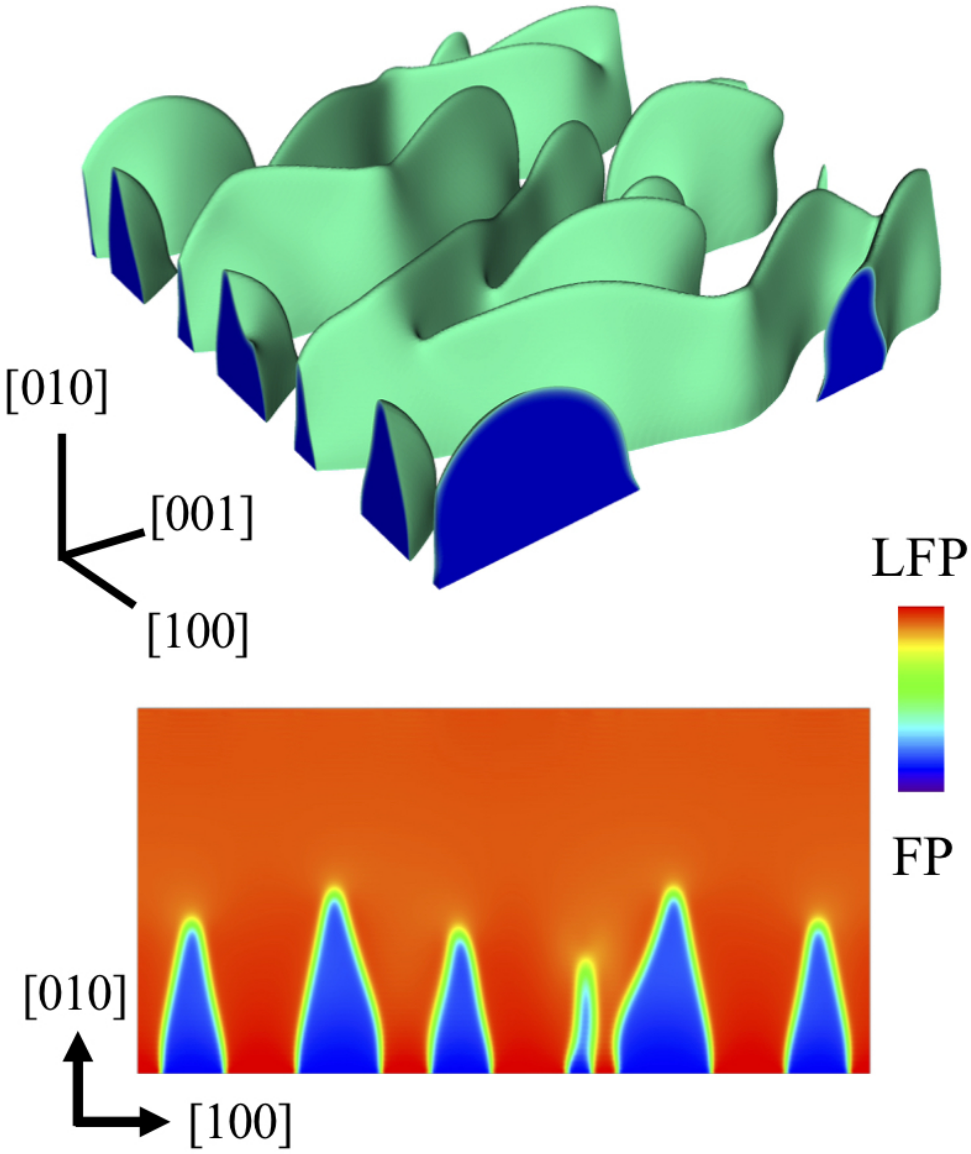

68x81mm (300 x 300 DPI)